INFLUENCE OF NEAR-SURFACE OXIDE LAYERS ON TIFE HYDROGENATION: MECHANISTIC INSIGHTS AND IMPLICATIONS FOR HYDROGEN STORAGE APPLICATIONS

Ⓘ **Archa Santhosh**[*]
Institute of Hydrogen Technology
Helmholtz-Zentrum Hereon
Max-Planck-Str. 1
21502 Geesthacht (Germany)
`archa.santhosh@hereon.de`

Ⓘ **ShinYoung Kang**, Ⓘ **Nathan Keilbart**, Ⓘ **Brandon C. Wood**
Laboratory for Energy Applications for the Future (LEAF)
Lawrence Livermore National Laboratory
Livermore, California 94550, USA

Ⓘ **Thomas Klassen**
Institute of Hydrogen Technology/Institute of Materials Technology
Helmholtz-Zentrum Hereon/Helmut-Schmidt-University
Max-Planck-Str. 1/Holstenhofweg 85
21502 Geesthacht/22043 Hamburg (Germany)

Ⓘ **Paul Jerabek**[*], **Martin Dornheim**
Institute of Hydrogen Technology
Helmholtz-Zentrum Hereon
Max-Planck-Str. 1
21502 Geesthacht (Germany)
`paul.jerabek@hereon.de`

May 17, 2023

ABSTRACT

The inevitable formation of passivating oxide films on the surface of the TiFe intermetallic compound limits its performance as a stationary hydrogen storage material. Extensive experimental efforts have been dedicated to the activation of TiFe, i.e. oxide layer removal prior to utilization for hydrogen storage. However, development of an efficient activation protocol necessitates a fundamental understanding of the composition and structure of the air-exposed surface and its interaction with hydrogen, which currently is absent. Therefore, in this study we explored the growth and nature of the oxide films on the most exposed TiFe surface (110) in depth using static and dynamic first-principles methods. We identified the lowest energy structures for six oxygen coverages up to approximately 1.12 nm of thickness with a global optimization method and studied the temperature effects and structural evolution of the oxide phases in detail via *ab-initio* molecular dynamics (AIMD). Based on structural similarity and coordination analysis, motifs for TiO_2, $TiFeO_3$ as well as $Ti(FeO_2)_x$ (x = 2, 3 or 5) phases were identified. On evaluating the interaction of the oxidized surface with hydrogen, a minimal energy barrier of 0.172 eV was predicted for H_2 dissociation while the H migration from the top of the oxidized surface to the bulk TiFe was limited by several high-lying energy barriers above 1.4 eV. Our mechanistic insights will prove themselves valuable for informed designs towards new activation methods of TiFe and related systems as hydrogen storage materials.

Keywords First-principles · Density Functional Theory · AIMD · Hydrogen Storage · TiFe · Oxide Layer · NEB · SOAP

1 Introduction

Driven by depleted resources and a drastic shift in climate conditions, there is an elevated attention on replacing conventional energy systems and utilizing sustainable, alternative renewable energy sources to their full potential. Hydrogen as an energy carrier takes up a leading role in this transitioning energy landscape.[1–3] When produced as "green hydrogen" from renewable sources, hydrogen energy systems offer low emission rates and are adaptable to

diverse operating conditions. Green hydrogen thus holds a key role in industrial decarbonisation and climate-neutral strategies released across the global energy economy.[4–6]

Efficiently storing hydrogen is pertinent to this goal of transforming our energy sector. A reliable choice of host material for solid-state hydrogen storage takes into account primarily the cost, storage capacity and the kinetics. The potential to tune pressure and temperature ranges, cycling stability and a higher volumetric capacity makes storage in metal hydrides especially attractive for stationary applications.[7] The intermetallic compound (IMC) titanium-iron (TiFe) is of large interest to the scientific community in this regard and represents one of the few materials that are already commercially utilized for integrated storage solutions.[8–10] TiFe remained relevant to stationary applications for over four decades owing to its cost-effectiveness and beneficial operating parameters under ambient conditions with a volumetric storage capacity of 0.096 Kg H_2/L.[11–16]

In theory, hydrogen molecule (H_2) dissociation and adsorption on the TiFe surface is a barrierless and thus fast process. This, however, only holds true for an ideal and clean TiFe surface.[17] Under realistic conditions, this reaction is hindered by several layers of passive oxide films on the surface.[12] The material thus has to undergo rigorous mechanical, chemical or thermochemical activation processes to facilitate hydrogen intake.[18–21] Attempting the complete removal of the TiFe oxide layers prior to activation (= first hydrogenation) so that hydrogen interacts only with the pristine metallic surface is a laborious process that is experimentally very challenging. A much more manageable goal for the activation of TiFe is facilitating hydrogen penetration through the near-surface oxide layers and oxide clusters present. One way of achieving this is by adding elements like Mn, Zr or Cr to the TiFe alloy that were found to be able to enhance the ability of hydrogen to penetrate the oxide and activate the storage material.[22,23] Substitutional elements are also thought to enhance initial hydrogenation rates at the surface by selectively forming oxides and secondary phases.[9,24] However, substitution may also lead to a capacity loss and the surface activated by heat treatment is again prone to deactivation upon air exposure.[11]

On the other hand, mechanisms of thermal activation have been discussed and analyzed to a large extent in literature, and there are currently two distinct proposed activation models that can summarize the general perspective:

1. Activation of air-exposed TiFe via the formation of TiO_2 and Fe clusters.[25,26] The precipitated Fe clusters provide a catalytic surface for H_2 dissociation

2. Segregated Ti-Fe-O oxide phases and clean TiFe surfaces formed freshly during desorption cycles provide catalytic means for H_2 intake.[12] No elemental Fe is formed in significant amounts

Evidences for both the presence and deficit of Fe clusters on the TiFe surface were found by means of magnetic measurements and Auger electron spectroscopy (AES) depth profiles.[27–31] The different findings on the nature of the oxide films and catalytic species facilitating H_2 intake imply that the surface-oxide formation and activation appear to be extremely sensitive to the experimental conditions, and hence hindering the establishment of a widely accepted model for TiFe initial activation.

Despite extensive experimental and theoretical investigations on this material, the oxidized surface has not yet been explored in depth on an atomistic level, although obtaining atomistic insights into the characteristics of the surface oxide films to better understand the underlying mechanisms is highly valuable to tune the material properties and activation kinetics for technical utilization of TiFe as storage material.

Thus, in this work, we seek to have a fundamental understanding of the early oxide-film growth on the IMC TiFe and its effect on H_2 interaction behavior by utilizing static and dynamic first-principles methods based on density functional theory (DFT). We will analyze the results with a focus on the appearing structural motifs, their influence on the energetics of hydrogen absorption into the bulk and possible implications for activation protocols of the storage material TiFe.

2   Methodology

Structural optimizations and energy calculations were carried out within the DFT framework as implemented in the Vienna *ab-initio* Simulation Package (VASP) version 5.4.4[32,33] with the revised version of Perdew–Burke–Ernzerhof functional for solids and surfaces (PBESol)[34] under generalized gradient approximation (GGA).[35,36] Projector augmented wave method (PAW)[37] pseudopotentials available with VASP were used to describe the core electrons and nuclei of the elements incorporating ten valence electrons for Ti ($3p^6 3d^3 4s^1$), eight valence electrons for Fe ($3d^7 4s^1$) and six valence electrons for O ($2s^2 2p^4$). An energy tolerance of 1×10^{-4} eV was set for convergence until the forces acting on atoms were ≤ 0.03 eV $Å^{-1}$. The static energy calculations employed a stricter energy tolerance of 1×10^{-5} eV and a **k**-mesh corresponding to 0.2 $Å^{-1}$ **k**-spacing. A plane-wave basis set energy cut-off of 450 eV was applied throughout. *Ab-initio* molecular dynamics (AIMD) calculations of the optimized structures or selected models were also

performed with VASP. All calculations were spin-polarized and a DFT-D3 dispersion correction scheme was used.[38] Based on the Hubbard model for a system of interacting electrons, an effective on-site Coulomb interaction parameter (U_{eff}) of 4.0 and 4.3 eV was applied to Ti and Fe, respectively (Except for the reaction energy barrier calculations, see below). The polyhedral models were visualized with VESTA 3.5.7.[39] All other structural representations were generated with Chemcraft 1.8 and graphical representations with the Matplotlib program.[40] For the ball-and-stick models, Ti, Fe, O and H atoms were given blue, grey, red and green colors, respectively, unless otherwise specified.
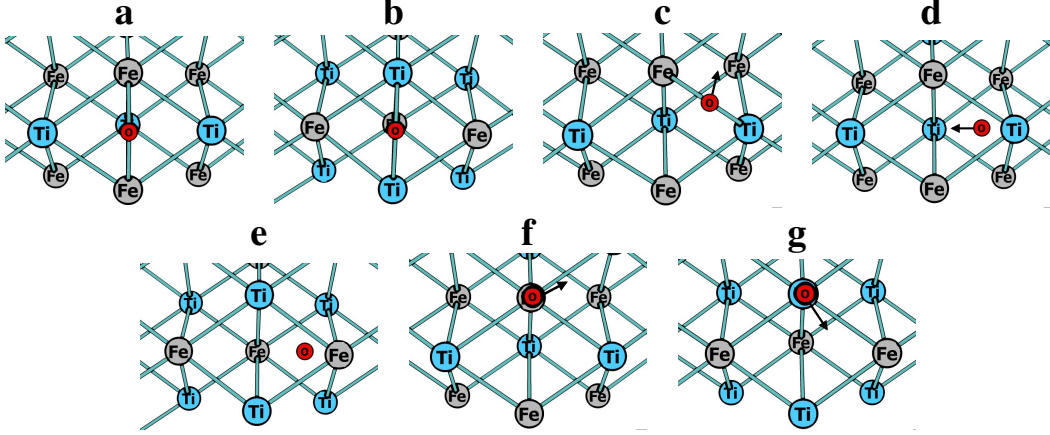

Figure 1: Oxygen adsorption sites on the TiFe (110) surface. Shown sites are (**a**) Fe-Fe bridge, (**b**) Ti-Ti bridge, (**c**) Ti-Fe bridge, (**d**) Fe-Fe-Ti threefold, (**e**) Ti-Ti-Fe threefold, (**f**) Fe on-top, and (**g**) Ti on-top.

2.1 Construction of oxidized TiFe surface models

In order to analyze the relevant TiFe surfaces, all orientations up to a maximum Miller index of three were processed with a Wulff construction[41] algorithm implemented in the Python Materials Genomics (pymatgen) library.[42] A 3×3 super-cell of TiFe in (110) orientation with 6-layer thickness (12.385 Å) containing 108 atoms was used for all the calculations. We kept a vacuum space of 24 Å between the surfaces. The basin-hopping (BH) global optimization method[43] was used to explore the energy landscape in order to identify stable low-energy structures of the oxidized TiFe surface for six different O coverages where the ratio between the O atom and surface metal atom = 1:1, 1.3:1, 1.8:1, 2:1, 2.4:1, and 3:1. A limited memory Broydon-Fletcher-Goldfarb-Shanno (LBFGS)[44] algorithm was used for local search, and the geometries of the identified structures were re-optimized with VASP to obtain a local minimum. A new structure was accepted or rejected depending on the energy difference from the previously accepted structure ($E_{\text{old}} - E_{\text{new}}$) with an acceptance probability (P) based on the Metropolis Monte Carlo criterion:[45]

$$P = \exp[(E_{\text{old}} - E_{\text{new}})/k_{\text{B}}T], \text{ if } E_{\text{new}} > E_{\text{old}}. \tag{1}$$

The last accepted local minimum was perturbed by a random number in the range $[-1, 1]$ and multiplied by a step-size of 0.1 Å for the next step. The BH runs were initiated from different starting points to ensure a lowest energy structure was obtained. The temperature was set to allow structure-sampling within an energy range of approximately 50 eV from the initial structure. (More details are available in the ESI)

2.2 Surface adsorption and binding calculations

The average energy of adsorption or binding of oxygen or hydrogen (E_{ad}) was calculated with Equation 2 where E_{ic} and E_{fc} are the total energy of initial and final configurations, respectively. E_{adatom} is the energy of one isolated oxygen or hydrogen atom and N is the number of atoms added. For calculating the average E_{ad}, the total energy of the clean TiFe surface was E_{ic} and the total energy of the surface after N atoms were adsorbed was E_{fc}.

$$E_{\text{ad}} = \frac{E_{\text{fc}} - (E_{\text{ic}} + N \times E_{\text{adatom}})}{N}. \tag{2}$$

For calculation of the coverage-dependent E_{ad}, we used the differential binding energy approach by taking the total energy of the previous configuration as E_{ic}.

2.3 Energy barrier calculations

The molecule dissociation and diffusion energy barriers (E_{act}) were calculated with climbing-image nudged elastic band (CI-NEB) theory and the force-based optimizers implemented in Transition State Tools for VASP (VTST).[46,47] The number of images were decided based on the distance between the initial and final states. For this study, three to five images were used when the distance between initial and final states was 2–6 Å. The atomic positions of the images were then relaxed until the forces orthogonal to the reaction path were lower than 0.02 eV Å^{-1}. Hubbard U-corrections were not used as they are known to cause numerical instabilities along the reaction pathways.[48–50] All other input parameters were the same as for the structural optimizations with VASP.

2.3.1 Hydrogen interaction with the interface between surface oxides and TiFe alloy

Hydrogen dissociation on the oxidized TiFe surface (3:1 ratio of O to surface metal atoms) was studied with the CI-NEB approach using the above mentioned settings. Based on the dissociation energetics and E_{ad}, H atoms were added to the top of the surface oxide layers and were allowed to relax to obtain surface models under hydrogen atmosphere.

In order to study the hydrogen binding and diffusion from the top of the oxide phases to the bulk interface region, 80 distinct configurations were generated by adding one H atom randomly at varying oxide-layer depths to the oxidized TiFe surface. The structures were allowed to freely relax in order to identify the preferred sites at different levels from the topmost region to the oxide/bulk interface region. This information was used to construct and assess the possible pathways for H to migrate through the surface oxide layers. The energetically most preferred migration paths in terms of the energy barriers were visualized.

2.4 Stability of O- and/or H-incorporated TiFe surfaces

From the energetics of the O and H adsorbed TiFe surfaces (Equations 2 and S2 in the ESI), a surface phase diagram was generated with the Surfinpy Python program[51] as a function of temperature and pressure.

$$\mu_X(T,p) = \mu_X(T,p^\circ) + 1/2 \ k_B T \ln(\frac{p}{p^\circ}) \tag{3}$$
$$\Delta\mu_X(T,p,p^\circ) = \mu_X(T,p) - \mu_X(T,p^\circ)$$

The chemical potentials (μ) of H and O, which are necessary to evaluate the relative stability of O and/or H-incorporated surfaces, were calculated with Equation 3, where X is the species, T is the temperature, p is the partial pressure and p° is the reference pressure (1 bar).[52,53] The temperature-dependent energy at 1 bar, $\mu_X(T,p^\circ)$, is the total energy of the respective species in a gas phase obtained from the NIST-JANAF thermochemical database.[54]

2.5 AIMD simulations for finite-temperature surface dynamics and structural analysis

Besides the basin-hopping global optimization method performed at 0 K, the properties of oxygen-contaminated TiFe surface at finite temperatures were further explored using AIMD simulations. The Nosé-Hoover thermostat was used to control the AIMD simulations within the canonical ensemble (NVT) to obtain insight into the impact of thermal treatment on the material.[55] For that, time steps between 0.5 and 1.0 fs were used and equilibration runs of at least 1 ps preceded the production runs. A Γ-only **k**-mesh was used for all AIMD runs.

For the obtained disordered surface structures, a subsequent coordination analysis to obtain information about the chemical environments of the atomic species was done with the ChemEnv Python module integrated with pymatgen.[56] Smooth Overlap of Atomic Positions (SOAP) descriptors as implemented in the DScribe Python package were used to find crystalline structural matches for the amorphous oxide layers within a radial cut-off of 2.6 Å. The degree of structural similarity between two atomic environments was characterized with a value from 0 to 1.[57–61]

3 Results and discussion

The optimized TiFe bulk structure was cleaved to obtain all distinct crystallographic planes up to a maximum Miller index of three. Table S1 (in the ESI) contains the respective surface formation energies and area fractions of surfaces of interest. The (110) surface forms with the lowest energy and has an area fraction of 57.2%, suggesting that it is the most preferred orientation for the TiFe IMC. This is in agreement with a previous theoretical study,[62] the (110) peak intensification observed in X-Ray diffraction (XRD),[16,63,64] and the transmission electron microscopy (TEM) analysis of TiFe lattice planes.[16,63,65] Therefore, in the following we focused on the (110) orientation as the most representative
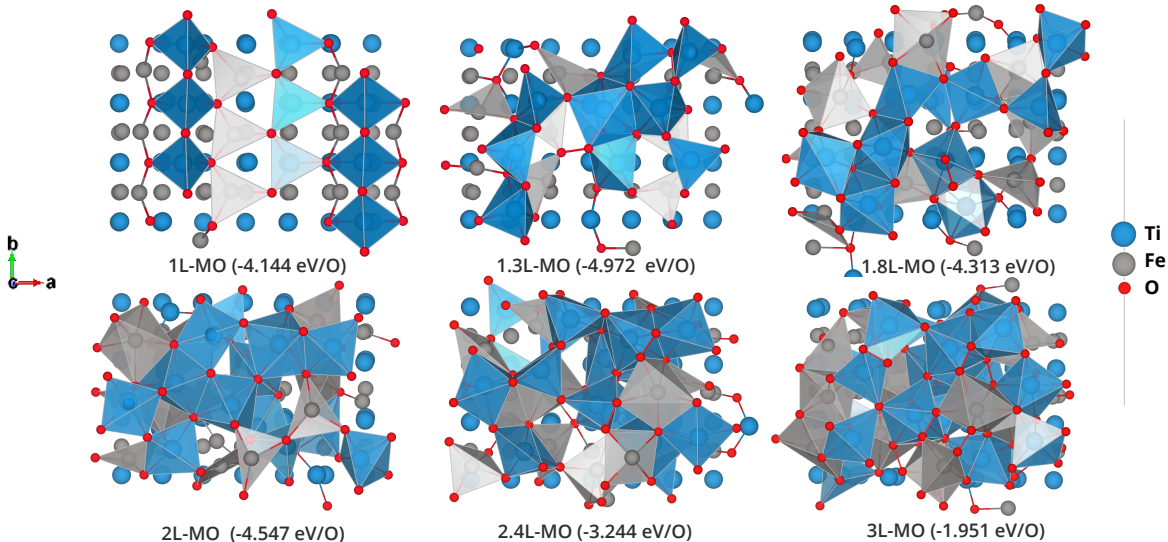
Figure 2: Oxide layer growth on the TiFe(110) surface with increasing oxygen content (O atom to surface metal ratio ranging from 1:1 to 3:1) depicted from a top-down perspective. In parentheses are the differential oxygen adsorption energies on the TiFe (110) surface with increasing oxygen content from the respective global minima identified via BH global optimization.

surface of TiFe. As passivating oxide films are almost always present under actual operating conditions of the material, we discuss oxide layer formation, stability energetics and dynamics based on the TiFe (110) surface in the following subsections.

3.1 Energetics of surface oxidation

3.1.1 Preferred adsorbtion sites for an oxygen atom

The pristine (110) surface is terminated with a 1:1 ratio of Ti and Fe atoms. We considered a total of nine possible coordination sites (Figure S3 in the ESI) for oxygen adsorption, namely the two metal on-top sites, three m_i-m_i and m_i-m_j bridge sites, and the four m_i-m_i-m_j threefold sites, where m_i = Ti or Fe atom and m_j is the other species. Figure 1 depicts and labels those seven sites (**a**)–(**g**) that we were able to identify as those leading to an energetically stable structures. (The remaining two long m_i-m_i-m_j threefold sites did not optimize towards such configurations.)

CI-NEB calculations carried out for O_2 dissociation resulted in a zero activation barrier on a clean surface: An oxygen molecule readily dissociates on the surface and adsorbs as atomic O on the described site. The corresponding adsorption energies (E_{ad}) were calculated by placing one O atom on the respective site and are given in Table 1. Here it can be seen that O preferentially adsorbs on the Ti-Ti bridge site (**b**) with E_{ad} = –5.497 eV/O, followed by the Ti-Ti-Fe threefold site (**e**) with –5.204 eV/O.

The Fe-Fe bridge site (**a**) is in principle also a stable site, but energetically clearly less preferred by $\approx$ 1 eV/O compared to the Ti-Ti bridge sites.

Table 1: Adsorption energies (in eV/O) at the preferred adsorption sites for an oxygen atom. The corresponding images are given in Fig. 1 labelled as **b**, **e** and **a**.

Surface site	Adsorption energy eV/O
Ti-Ti bridge (**b**)	–5.497
Ti-Ti-Fe threefold (**e**)	–5.204
Fe-Fe bridge (**a**)	–4.528

When an oxygen atom is placed on the other sites, i.e. (**c**), (**d**), (**f**) and (**g**), the O adatom moves to one of the above mentioned preferred sites in the direction given as arrows depicted in Figure 1. We found that increasing O content on

5

the surface is capable to energetically stabilize oxygen absorption at these sites, however, we were unable to obtain E_{ad} by constraining the adsorbed O atom at these sites since it caused surface buckling.

3.1.2 Coverage-dependent oxide layer stability

We proceed to the assessment of the coverage-dependent stability of the oxidized surface. In our definition, a single monolayer oxide film corresponds to one O atom per metal site on the surface and is labelled as 1L-MO. The number of the monolayer metal oxide (MO) films was labelled as nL-MO with n indicating the ratio between O atoms and surface metal atoms. We were able to study the effects of systematic oxygen content increase up to 3L-MO (i.e. a 3:1 ratio between O and surface metal atoms).

The respective stable atomic configurations were identified by the BH global optimization method, which means that unlike the usual relaxation of a single structure to its local minimum, a Monte-Carlo minimization method was used that searched through several local minima in order to identify the global minimum. From at least 100 stable configurations explored at six different oxygen concentrations (1L-ML to 3L-MO), the lowest energy structures at each respective oxygen concentration were selected and studied further. The corresponding adsorption energies as the oxygen content in the surface layer grows are shown in Figure 2.

The first oxide layer (1L-MO) forms spontaneously upon oxygen exposure with an average adsorption energy of –4.144 eV/O. Adding more oxygen atoms to the surface layer does not significantly penalize the energy cost until 2L-MO (–4.547 eV/O), which means that two layers of oxygen atoms can be effortlessly formed on pristine TiFe. Upon reaching a 2.4:1 ratio between O and surface metal atoms, the adsorption energy starts to become more positive (–3.244 eV/O for 2.4L-MO) and reaches –1.951 eV/O as the third layer (3L-MO) is formed, showing a noticeable decrease in oxidation tendency.

Visual inspection in Figure 2 reveals that with addition of the third oxygen monolayer, the pristine intermetallic surface is entirely covered with amorphous oxide phases forming an interface between bulk TiFe and its oxygen exposed surface. We want to note that we observed their appearance already in conventional DFT optimizations of the oxide surface models, from which can be concluded that clustering of these phases forming cavities in the subsurface region is present already at 0 K (as can be seen in Figure S4 in the ESI).

Due to the system size, we found studying the addition of a higher oxygen content beyond 3:1 to be computationally prohibitively expensive. However, an excess-O_2 model is discussed in Section 3.3 to predict further O_2 reactions with the final model.

3.2 Hydrogenation energetics of oxidized surface

3.2.1 Dissociation and adsorption of hydrogen on the O-contaminated surface

In order to investigate the reactivity of the fully oxidized TiFe surface towards hydrogen, H_2 molecules were added to the 3L-MO system obtained from BH optimization and the reaction energy barriers for hydrogen dissociation at three different types of sites were computed using CI-NEB. For that, H_2 was placed in different orientations with respect to the TiFe surface on top of each surface-exposed O, Fe or Ti atom in 3L-MO. These served as the respective initial configurations for a series of NEB calculations that explored the energy pathways and activation barriers for hydrogen dissociation and H adsorption at the surface. In the following we discuss the lowest energy barriers from our investigations found for each of the dissociation sites (O, Ti and Fe, respectively).

For the process of dissociating H_2 placed on top of an oxygen atom and successive adsorption at the same O atom, we find a rather high barrier of ≈ 2.0 eV. Dissociating hydrogen at a Ti site lowers this energy slightly to around 1.9 eV. Interestingly, a very low activation barrier of only ≈ 0.17 eV along with a strong adsorption energy of –3.0 eV is observed for dissociation on top of an Fe site (here, H_2 was initially oriented orthogonal to the surface). The corresponding minimum energy path is plotted in Figure 3 along with the initial and final configurations. (The paths for the O and Ti sites are shown in Figure S5 in the ESI).

Since an energy barrier of 0.17 eV is readily accessible at experimental conditions, it will be very easy for H_2 molecules to dissociate and adsorb at these positions. Note that the Fe atom in this case is not part of a segregated iron cluster (as postulated earlier for the first activation model), but is a part of a metal oxide layer.

Because of the rather low H_2 dissociation barrier and strong adsorption energy at the investigated Fe site, we can assume that under hydrogen atmosphere a large amount of H atoms must be present close to and within the metal oxide layer. We therefore decided to test the 3L-MO model further by placing an increasing amount of H atoms to the top surface layer and performed conventional structure optimizations to investigate their adsorption energies. H atoms were initially placed close to the exposed Fe sites, followed by Ti or O sites and were allowed to freely relax.
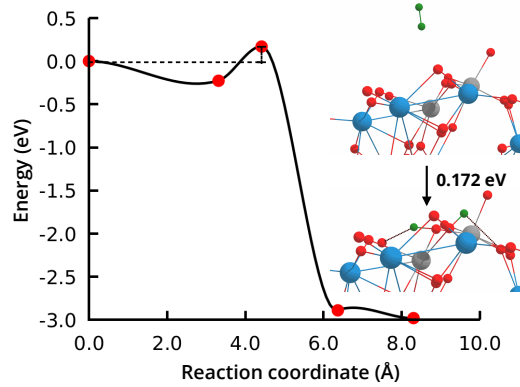
Figure 3: Energetically most favorable minimum energy path we explored for hydrogen molecule (green) dissociation and adsorption at the 3L-MO surface. The H_2 molecule was placed on top of a Fe site (gray) in orthogonal orientation with respect to the TiFe surface at the initial configuration. The path and energy barrier (0.172 eV) are obtained from CI-NEB calculations.

The H adsorbed nL-MO system is referred to as nL-MO:mH, where m is the number of H atoms added. The average adsorption energies indicate high stability for adsorption of 2 to 20H atoms, and its stability weakens to –0.639 eV/H when the H content further increases up to 28H (Table 2).
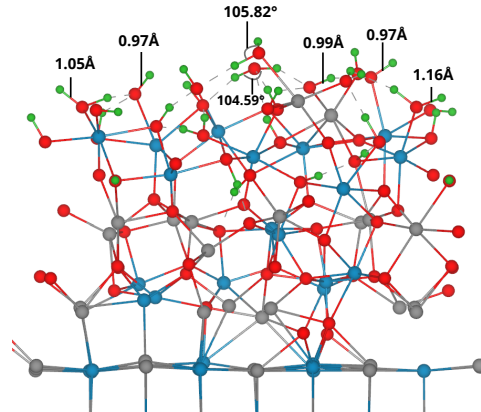

Figure 4: H adsorption on the 3L-MO surface (3L-MO:28H model). Relevant O-H distances and H-O-H angles at the top surface are labeled. (The O-H bond length and the H-O-H bond angle for an isolated water molecule is 0.97 Å and 104.5°, respectively.) Atomic sizes are reduced for a clearer representation.

Table 2: Average hydrogen adsorption energies (eV/H) on the 3L-MO surface.

m**H**	**2H**	**16H**	**20H**	**24H**	**28H**
$\mathbf{E}_{ad}$ **(eV/H)**	– 2.956	– 1.354	– 1.126	– 0.766	– 0.639

It was observed that increasing hydrogen content eventually leads to the formation of hydroxyl (OH^-) and water (H_2O) moieties as H preferentially binds to the O sites of 3L-MO (see Figure 4). Both species, OH^- and H_2O, are chemically stable and could be utilized for oxygen removal from the oxide layer. The conditions under which these groups could in principle get removed from the surface is analyzed in detail via AIMD in Section 3.3.2.

Regions favoring oxide growth and/or hydrogen binding are formed at the TiFe surface depending on the respective H/O partial pressure, the chemical potential difference ($\Delta\mu$) being decisive here in the growth of any particular environment. The relative stability of these surface structures is visualized as a surface phase diagram in Figure 5 as a function of $\Delta\mu$

7

at 298 K. For that, $\Delta\mu$ at 0 K was extended to correspond to standard temperature (298.15 K) using experimental data from the NIST-JANAF thermochemical database applying the relation shown in Equation 3.
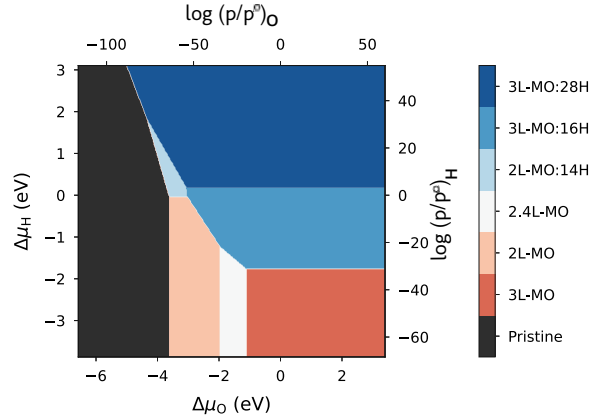

Figure 5: Surface phase diagram showing the thermodynamic stability of different surface compositions as a function of O and H chemical potential differences ($\Delta\mu_O$ and $\Delta\mu_H$) at 298 K.

From the diagram, in Figure 5 can be seen that at very low chemical potentials for H and O, the 2L-MO system is in equilibrium with the pristine TiFe surface. However, as the O chemical potential rises (corresponding to a growing oxygen partial pressure), the oxygen content on the TiFe surface gradually increases, and finally the 3L-MO system becomes energetically more favorable and is the dominant surface for technically relevant pressures (i.e. ≥ 1 bar). When the chemical potential/partial pressure of hydrogen is taken into account, we can see that 3L-MO:16H represents the relevant surface model at moderate H partial pressures of ≤ 1 bar, and 3L-MO:28H becomes the dominant surface for higher H pressure.

3.2.2 Hydrogen penetration to the bulk

Although the exact mechanisms are not yet fully understood, it is clear that hydrogen diffusion is the rate-limiting step during the activation process of TiFe. Since this aspect plays such a major role, we want to establish a useful reference by a detailed description of the H diffusion through the Ti-Fe-O amorphous oxide layer prior to thermochemical treatment of the generated material and before adding any dopants to TiFe so that their role can be better determined in future experimental or theoretical investigations.
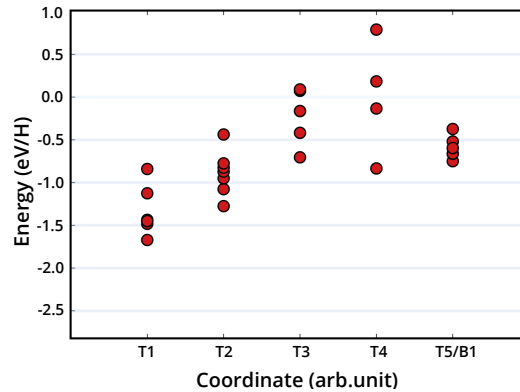

Figure 6: Binding energies for H as a function of distance from the top surface (T1) to the near-bulk layer (T5/B1) in the 3L-MO:1H model. Red circles represent possible binding sites at each depth level.

The 3L-MO:1H model can be understood as a very low hydrogen exposure for the oxidized surface and therefore corresponds to the very early moments during hydrogenation. H binding to 80 distinct sites of the amorphous TiFe
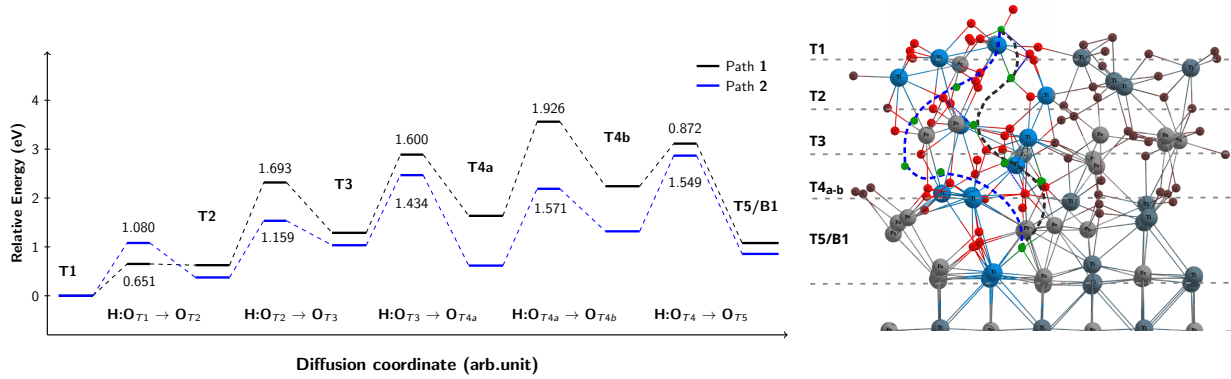
Figure 7: Hydrogen diffusion through the oxidized TiFe(110) surface using the 3L-MO:1H model. The minimum energy paths through each of the oxide subsurface layers T1–T5/B1 are given with the corresponding activation energy barriers from NEB calculations. The resulting trajectory paths for hydrogen (green) from T1 to T5/B1 is visualized on the right as a dashed grey (Path **1**) and dashed blue line (Path **2**). To lead the eye, the oxygen atoms not relevant for the hydrogen paths are in brown.

oxide structure was evaluated using this model in order to map out the possible migration paths to the bulk of the structure (see Methodology section).

Based on the energies and stable configurations of one hydrogen atom added to the respective binding sites, the surface oxide can be divided into five depth levels through which H has to pass in order to reach the bulk of TiFe. Figure 6 summarizes the binding in an energy range between –1.67 eV/H (most favorable site at level T1) and +0.79 eV/H (least favorable site at level T4). The coordinates T1–T5 indicate the distance from the top level: T1 is the topmost surface layer and T5/B1 stands for the deepest layer/near-bulk interface region in the structure, while T2–T4 are the intermediate layers. The different depth levels are visualized in the right part of Figure 7.

Interestingly, the hydrogen binding in the oxidized 3L-MO:1H system is most preferred on the topmost surface (T1), becomes energetically less favorable in proportion with the distance from the top surface (T2–T4), and stabilizes again when near to the oxide/TiFe alloy interface (T5/B1). The respective binding positions can be characterized as oxygen sites for T1–T4 and metallic for T5/B1.

From several possible migration paths investigated based on the hydrogen binding energies (see Table S2 in the ESI), the two energetically most likely migration paths, Path **1** and Path **2**, for one hydrogen atom to reach the T5/B1 layer starting from the T1 layer is plotted in Figure 7 together with the corresponding activation energy barriers (E_{act}) from NEB calculations. Figure 7 shows that for Path **1**, diffusion from one O site in the T1 layer to another in the T2 layer (H:$O_{T1} \to O_{T2}$) only requires an E_{act} of 0.651 eV. E_{act} for H:$O_{T1} \to O_{T2}$ is slightly higher at 1.080 eV for Path **2**. For moving hydrogen from T2 via T3 to T4a, the energy barriers increase noticeably for both pathways. This can be understood by considering that on the top layers the oxide phases are more clustered, forming larger cavities which results in less hindrance to H movement from T1 to T2.

As can be seen from Figure 6, there are less favorable H binding sites in the T4 layer. Moreover, E_{act} for movement within the T4 region (H:$O_{T4a} \to O_{T4b}$) possesses the highest energy barrier found along any one path (1.926 eV for Path **1** and 1.571 eV for Path **2**). Interestingly, the H migration from the oxygen-neighboring site in the T4b layer to an intermetallic site in the T5/B1 layer (H:$O_{T4a} \to M_{T5/B1}$) at the interface takes place with an energy release, –1.385 eV and –0.462 eV, respectively, for Paths **1** and **2**. Since the reaction energy to go from T4 layer to T5/B1 is exothermic, it can be assumed that the H atom is unlikely to travel back into the oxide layer after the final migration step. At the same time, the high-lying energy barriers from T2 to T4 also indicates that the H atom could get trapped in the oxide layers before hydriding the alloy.

After analyzing the energy profile for the migration path in its entirety, we state the following observations:

1. The total reaction energy for migrating H from the top-most layer to the bulk/interface layer is 0.854 eV for Path **1** and 0.356 eV for Path **2** and thus the process is endothermic in nature.

2. In order to reach the oxide/bulk interface layer from the top-most layer, several high-lying energy barriers ($\approx$1.2–1.9 eV) need to be overcome.

9

Table 3: Sampled hydrogen diffusion pathways and the corresponding reaction energies ΔE and barriers E_{act} (in eV/H). The overall reaction energies (ΔE_{tot}) for each path are also given in brackets

Path	Migration type	ΔE	E_{act}
1 3L-MO:1H (ΔE_{tot}=0.854 eV)	H:$O_{T1} \rightarrow O_{T2}$	0.623	0.651
	H:$O_{T2} \rightarrow O_{T3}$	0.662	1.693
	H:$O_{T3} \rightarrow O_{T4a}$	0.348	1.600
	H:$O_{T4a} \rightarrow O_{T4b}$	0.606	1.926
	H:$O_{T4b} \rightarrow M_{T5/B1}$	−1.385	0.872
2 3L-MO:1H (ΔE_{tot}=0.356 eV)	H:$O_{T1} \rightarrow O_{T2}$	0.405	1.080
	H:$O_{T2} \rightarrow O_{T3}$	0.659	1.159
	H:$O_{T3} \rightarrow O_{T4a}$	−0.417	1.434
	H:$O_{T4a} \rightarrow O_{T4b}$	0.171	1.571
	H:$O_{T4b} \rightarrow M_{T5/B1}$	−0.462	1.549
3 3L-MO:10H (ΔE_{tot}=1.469 eV)	H:$O_{T1} \rightarrow O_{T2}$	0.183	0.958
	H:$O_{T2} \rightarrow O_{T4}$	−0.393	1.733
	H:$O_{T4} \rightarrow M_{B1}$	1.679	2.272

A general rule of thumb from kinetics states that at room temperature only reactions with activation barriers below $\approx$ 85 kJ/mol (0.8–0.9 eV) will result in a reasonable rate constant. Since the reactions up to T4 are endothermic, the reverse paths possess even lower barriers making a back migration out of the oxide layer highly likely at room temperature.

In addition to the single H atom migration paths discussed above, we also investigated hydrogen migration energetics in the presence of multiple H atoms using the 3L-MO:10H system, which are labelled as Path **3** in Table 3. (The corresponding reaction pathways are shown in Figure S6 in the ESI.)

Due to the structural changes caused by increased the H content, the hydrogen atom can hop farther between the oxide layers in single steps. Thus, it is possible that one H can reach the oxide/bulk interface in three steps in Path **3**. However, to achieve this, the overall reaction becomes much more endothermic (1.469 eV) than the five-step migrations in Paths **1** and **2**. Although the initial activation barrier is relatively low (0.958 eV) and the one-step migration from T2 to T4 is exothermic, the migration into the oxide/TiFe interface from the T4 layer requires a very high E_{act} of 2.272 eV and is endothermic, further hinting at hydrogen trapping in the oxide layers at moderate temperatures.

We conclude this part by stating that our findings are consistent with the experimental observation that hydrogen does not sufficiently penetrate TiFe oxide layer under standard conditions. According to our calculated hydrogen migration energetics the initial hydrogenation process therefore requires one or several of the following approaches:

- Significant increase in reaction temperature to overcome the high activation barriers
- A high hydrogen concentration to increase the chances of H atoms migrating through the oxide layer in fewer steps
- Utilization of catalytically active dopants to lower the activation barriers

3.3 Oxide speciation analysis via finite-temperature molecular dynamics simulations

In the following, the dynamic stability and structural evolution with temperature of the three oxide layer models (1L-MO, 2L-MO and 3L-MO) as well as the effect of hydrogen addition (3L-MO:28H) on the top oxide layers were explored via AIMD simulations. An X-ray photoelectron spectroscopy (XPS) study by L. Schlapbach and T. Riesterer determined an oxide layer thickness of less than 2 nm on fractured TiFe, which is comparable to the extension of the oxide layer on our 3L-MO model that spans about 1.12 nm of the surface. However, we want to note that oxygen-rich films of up to 20 nm thickness can be generally observed on the material surface according to other studies.[23,66]

Starting from DFT optimized structures in Section 3.1.2, the simulation temperatures were increased in steps of 150 K beginning from 300 K (room temperature) up to 600 K for a time duration of 5 and 10 ps at each temperature to obtain thermally calibrated oxide phases.

One of our goals was to estimate how much more oxygen can potentially react with the surface at experimental conditions. For that, we introduced six excess oxygen molecules close to the 3L-MO surface and analyzed the occurring

reactions over an extended simulation time period of 20 ps at 300 K and 673 K, respectively. For both temperatures we found that only three more oxygen molecules dissociated and attached to the surface layer. The remaining oxygen molecules appeared only weakly adsorbed to the top of the oxide layer without showing any integration into the oxide itself. Snapshots of the AIMD simulation run at 673 K depicting this are shown in Figure S7 in the ESI. The interaction between the O_2 moieties and the oxide layer appeared not to be very strong and we could observe in the higher-temperature simulation runs that the attached O_2 groups left the oxide layer and were released as oxygen molecules again.

From these results, it can be concluded that most of the oxygen molecules are only rather weakly physically adsorbed on the air-exposed surface and can potentially be easily removed by low-temperature activation methods, such as those mentioned by Dreistadt et al.[23] or Patel et al.[67] Moreover, it shows that the three oxide layer thickness considered in this study offers a suitable primary depiction of the air-exposed TiFe for the intended technical purpose as room-temperature hydrogen storage material. Therefore, we proceeded to assess the stability and chemical environment of the near-surface oxides using the obtained AIMD data.
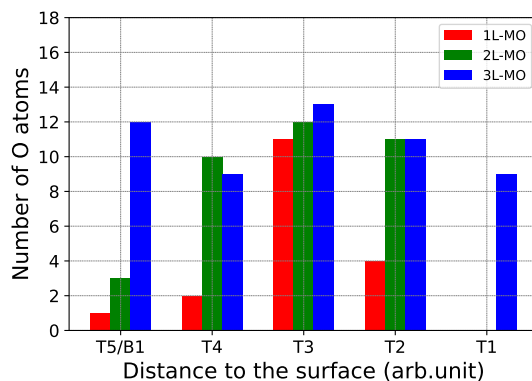

Figure 8: Number of oxygen atoms present at each depth level from near-bulk (T5/B1) to top-most layer (T1) in the 1L-,2L- and 3L-MO models after AIMD simulation runs (10 ps at 600 K).

After a simulation period of 10 ps at 600 K, an interface between the TiFe surface and the amorphous oxide layer is evident in the 1L, 2L and 3L-MO models. To get a clearer picture of where the oxygen atoms accumulate in the respective systems, the number of O atoms as a function of distance to the top surface (defined as T5/B1 to T1 as seen in Figure 7) is plotted in Figure 8. In addition to the general non-uniformity of the growing oxide layer, we can also observe that for all three models, oxygen is clustered mostly at the T3 level. For the 1L and 2L models, this effect is especially pronounced resulting in almost no O atoms being present in the interface region (T5/B1) and the top-most layer (T1).

3.3.1 Oxide structure match with SOAP

In order to offer a better description of the chemical environment within the near-surface oxide layers, the end structures from 10 ps AIMD simulations at and above 600 K were selected to identify and categorize the different Ti-Fe-O species on the oxygen contaminated surface. Unlike crystalline solids with a long-range order, however, the structure of these oxide films can only be quantified in limited parameters.

Therefore, we employed the SOAP descriptor to characterize the local chemical environment of the amorphous oxide layers. This method is proven to give discerning structural descriptions that can be used to find matches utilizing a structural similarity value between 0 (no similarity) and 1 (highest possible similarity).[68]

The SOAP vectors generated from the AIMD structures were compared with all documented Ti-Fe-O phases from the Materials Project database.[69] All identified crystalline structures for the three different oxide layer models on the surface at different simulation temperatures (300 K, 600 K, and 750 K) at given in Table S3 in the ESI. The dominant phases with similarity values >0.6 are visualized in the ternary diagrams in Figure 9.

For the models with increased oxygen content we find high similarities with Ti_2FeO_5 (2L-MO, 600 K: 0.7675; 3L-MO, 600 K: 0.8684) and $TiFe_2O_5$ (2L-MO, 600 K: 0.7663; 3L-MO, 600 K: 0.8667). Motifs for Ti/Fe-O phases such as TiO_2 (3L-MO, 600 K: 0.7451), Fe_2O_3 (3L-MO, 600 K: 0.7428) and Fe_3O_4 (3L-MO, 600 K: 0.7426) can also be observed.

(a) 1L-MO:600K

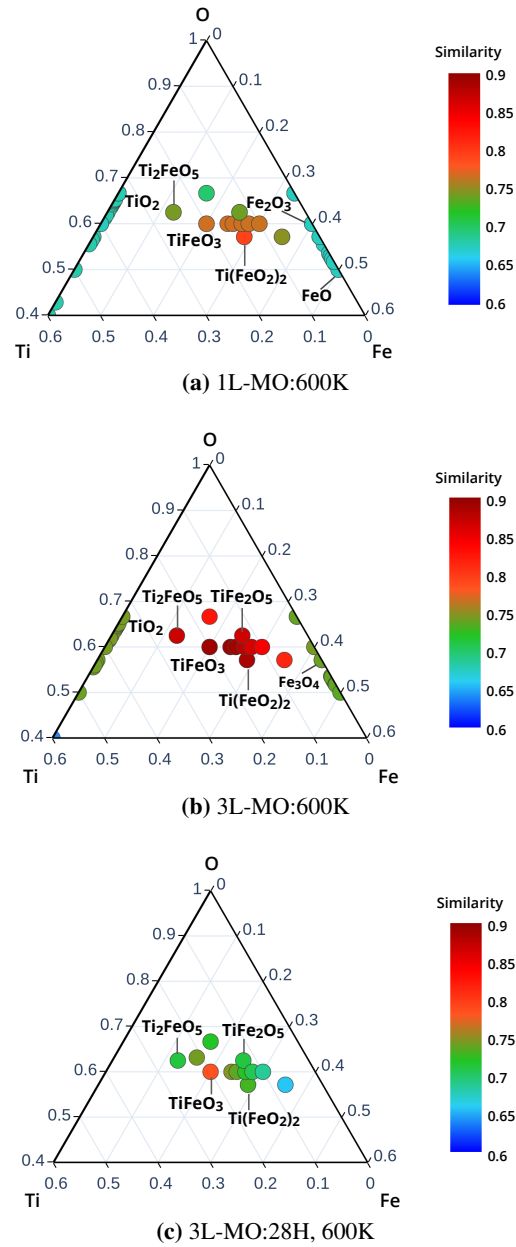
(b) 3L-MO:600K

(c) 3L-MO:28H, 600K

Figure 9: Structural matches identified for the oxide films 1L-MO, 3L-MO and 3L-MO:28H with SOAP descriptors. The relevant phases above a similarity value of 0.6 are labelled in the ternary diagrams.

In general, the $TiFeO_3$ structural motif appears consistently throughout the models: As the oxygen content increases, the structural similarity with $TiFeO_3$ increases from 0.7702 (1L-MO, 600 K) to 0.7939 (2L-MO, 600 K) and finally 0.8949 (3L-MO, 600 K). It is also the best experimentally observed structural match obtained for all three models.

Moreover, the structural similarity value of 3L-MO with the $TiFeO_3$ phase rises to 0.9470 at 750 K (Table S3 in the ESI). This indicates a stabilization of this phase with increasing temperature, which implies that further studying $TiFeO_3$ might be important for high-temperature activation methods.

Whilst introducing hydrogen to the top oxide layers of 3L-MO at 600 K (3L-MO:28H, 600 K) clearly reduces the Ti-Fe-O structural matches (Ti_2FeO_5: similarity of 0.7117; $TiFe_2O_5$: similarity of 0.7111), the similarity to $TiFeO_3$ remains high at a value of 0.7840 (Figure 9c).

12

Furthermore, we expanded the database to include H species for the 3L-MO:28H model analysis at 600 K and identified the best matches with $FeHO_2$ (similarity of 0.7908) and $Fe(OH)_2$ (similarity of 0.7908). Several unstable phases were detected as well, such as $Ti_2H_2O_3$ that decomposes to TiO_2, TiH_2 and H_2; $Ti_3H_2O_7$ that decomposes to TiO_2 and H_2; and $Ti(OH)_2$ that decomposes to TiO_2 and H_2O. The structural similarity values of any single Ti/Fe-O phase were found to be <0.6 and hence were omitted from Figure 9c.

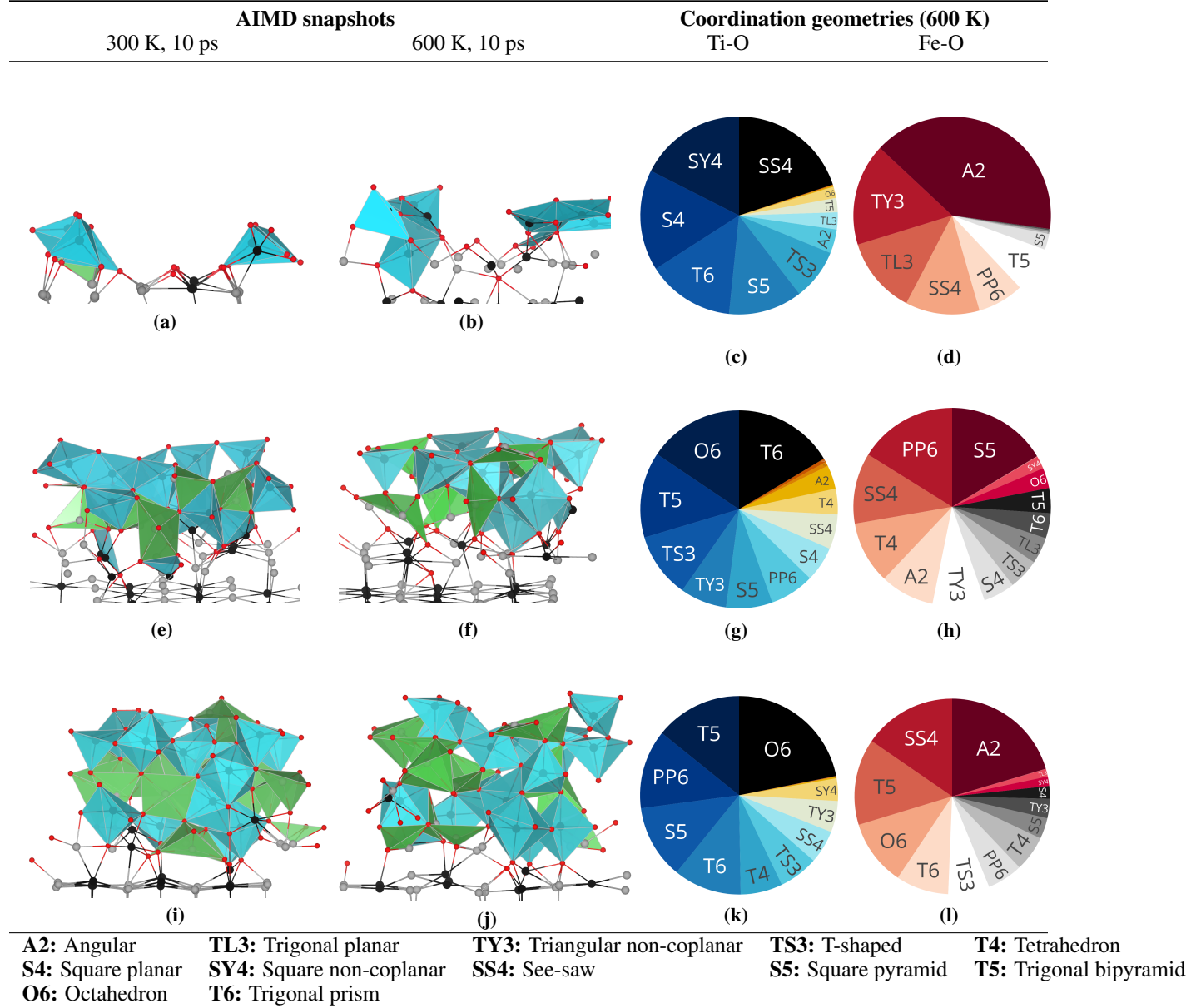| A2: Angular | TL3: Trigonal planar | TY3: Triangular non-coplanar | TS3: T-shaped | T4: Tetrahedron |
| S4: Square planar | SY4: Square non-coplanar | SS4: See-saw | S5: Square pyramid | T5: Trigonal bipyramid |
| O6: Octahedron | T6: Trigonal prism | | | |

Figure 10: Structural evolution of the amorphous oxide layer is visualized in polyhedral models at oxygen coverages from 1L (a-d), 2L (e-h) to 3L (i-l). Blue and green polyhedra correspond to Ti and Fe coordination, respectively. Ti and Fe atoms are drawn as black and grey spheres to highlight the polyhedra. Pie charts of coordination geometries are given for Ti/Fe-O coordinations at 600 K for each oxygen coverage. The label of the coordination geometry in each pie chart consists of the symbol and corresponding CN. (The naming is adopted from a study by Waroquiers et al.[56] and listed below.)

3.3.2 Local coordination analysis

Despite the several crystalline phases we identified from the similarity structure match, an oxygen contamination under real conditions may not always meet the kinetic and thermodynamic conditions to form surface oxides that are structurally close to the investigated crystalline oxides, but rather lead to more disordered and dispersed sub-stoichiometric species.

Therefore, in addition to the structure match, a statistical search of all local coordination geometries of the surface oxide phases were performed to characterize the oxygen-incorporating local environments of the metal atoms.

The Ti-O and Fe-O coordination was analyzed using the 1L-, 2L- and 3L-MO models at a maximum cut-off distance of 2.6 Å
and upto a coordination number (CN) of 6. The trends in CN(M-O) and morphology plotted in Figure 10 can further shed light into appearing structural motifs: For the 1L-MO system, after a simulation period of 10 ps at 600 K, Ti is coordinated to mostly four oxygen atoms in seesaw (SS4), square-planar (S4) or square non-coplanar (SY4) geometry, whereas the majority of Fe is surrounded by two or three oxygen atoms represented by angular (A2), triangular non-coplanar (TY3) or distorted trigonal planar (TL3) geometry. As Ti gets preferentially oxidized, it is lifted out of the bulk surface as can be seen from Figure 10b.

Continuing with 2L-MO, the increase in O content leads to higher CN(Ti) and CN(Fe) and we can find corner-sharing trigonal bipyramids (T5) in TiO_5 units on the top layers with three shorter and two longer Ti-O bonds varying from 1.86 Å to 2.16 Å. About 14% of Ti sites are in the T5 coordination. The 6-coordinated geometry is dominating with trigonal prismatic (T6) and octahedral (O6) coordination (16.4% and 15.6%, respectively). Distorted 3-coordinate environments, such as the T-shaped (TS3) and the trigonal planar (TY3) geometries, are also formed on the oxide layer close to the bulk interface (Figure 10g). On the other hand, at this stage about 16.5% of the Fe sites are coordinated in square pyramidal (S5) geometry and 4.1% of Fe sites are in trigonal bipyramidal (T5) geometry sharing a corner O atom with TiO_5 or TiO_6 units as in the $TiFeO_3$ phase.
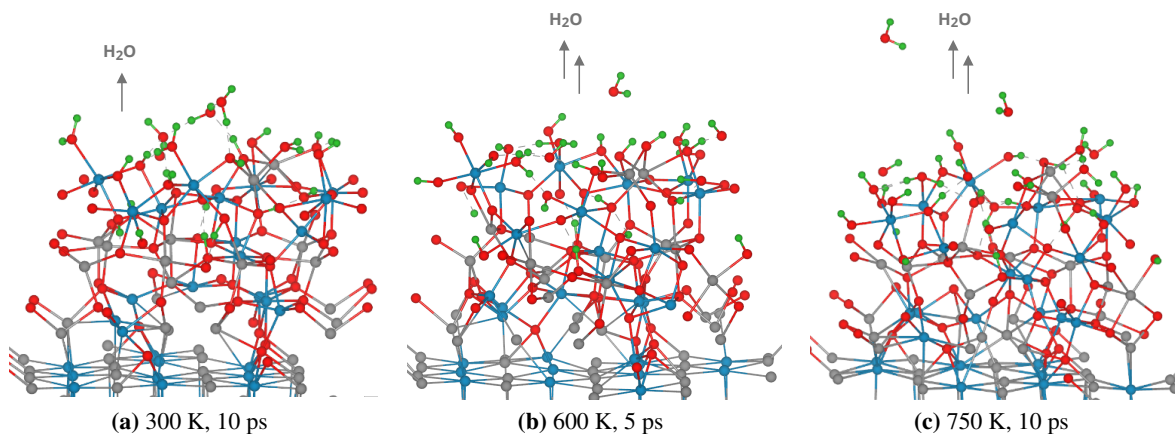

Figure 11: AIMD snapshots of 3L-MO:28H model at different simulation temperatures. Physisorbed H_2O molecules can be seen moving away from the surface as the simulations progress and the systems anneal.

With introduction of the third oxide layer (3L-MO), the octahedral (O6) Ti sites increase to 21.9% along with trigonal bipyramidal (T5) sites (14.2%). The octahedral units are slightly distorted and mostly share an edge O with T5-coordinated Ti sites and a corner O with T5-coordinated Fe sites. Although a larger fraction (20.4%) of Fe atoms are found to have 2 oxygen neighbors in A2 geometry, a significant increase in units with CN=5 and 6, such as T5 (14.3%) and O6 (10.9%), can also be observed.

The generally observed trend is that with higher oxygen content (1L-MO → 3L-MO) higher CN(M-O) values for Ti (from 4 up to 6) and Fe (from 2 up to 6) are realized, which matches well with chemical intuition.

Variations in local coordination in the different surface compositions are further represented by the radial pair distribution function (RDF) plotted in Figure S9 in the ESI. Note that the first Ti-O peak locations between 1.95 Å and 2.05 Å are characteristic for amorphous TiO_2,[70,71] which can be assigned with an average CN(Ti-O)=5–6 from the coordination analysis. The increasing fraction of O6-coordination from 1L- to 3L-MO (Figure 10) and the general structural motif of Ti coordinated with 5 or 6 O atoms is also indicative of TiO_2 phase formation in extended time periods.

14

The first Fe-O peak (between 1.95 Å and 2.05 Å) appears at the same distance as the Ti-O peak in the 1L-MO and 2L-MO model (Figure S9) but shifts slightly to 2.05–2.15 Å in the 3L-MO RDF. Analysis of these peaks (Ti/Fe-O) together with the observed increase in the corner-sharing O6 Ti-O and T5 Fe-O geometries suggest the formation of $TiFeO_3$ phase-like motifs in models with higher oxygen content, which is in agreement with the structural similarity analysis via SOAP in the previous part.

Finally, the interaction of the amorphous surface oxides with hydrogen at different temperatures were studied using the 3L-MO:28H model for a duration of up to 20 ps with AIMD. We found that the high content of O and H results in the formation of H_2O moieties on the surface. A summary of the O–H bond lengths and H–O–H bond angles is given in Table S3 in the ESI. At 300 K and after 10 ps, H_2O groups are found physisorbed to the top surface with a mean H–O–H bond angle of 107.32°. At 750 K the mean bond angle decreases to 104.63°, getting close to that of an isolated H_2O molecule. This implies that the interaction between the surface oxides and most of the H_2O moieties are rather weak, which likely enables their removal. This is also evident as H_2O groups on the surface move farther away as the temperature increases and/or as the simulation progresses (Figure 11).

An overview of the Ti and Fe coordination environments of the 3L-MO:28H model at 600 K is plotted in Figure S10 in the ESI. A very large fraction of Ti (40.1%) is found in O6 coordination while most of Fe (20.1%) is in A2 coordination. The CN of Fe decreases as a result of reduction through the introduction of hydrogen into the system as well as the appearance of titanium oxide phases like TiO_2.

From the analysis of the chemical environment analysis and the RDF in Figure S9, we conclude that the top oxide layers under H-rich environment are likely composed of motifs from $FeHO_2$, $Ti_3H_2O_7$, $TiFeO_3$ and TiO_2 amorphous phases. Adsorbed H reduces the surface oxides but is not altering the general RDF at 600 K.

3.4 Mechanistic insights

From the detailed analysis of the chemical environment of the oxidized TiFe surface using structural similarity matching, local coordination analysis and RDF approaches in conjunction with an in-depth description of the energetics to penetrate the near-surface oxide layers with hydrogen, we can summarize our findings and insights into the mechanisms of surface oxide growth and initial hydrogenation as follows:

1. Preferential oxidation of Ti over Fe is evident in all oxidation stages from the coordination analysis.

2. Clustering of metallic Fe is not directly observed in the studied temperature range of 300–750 K. However, this could also be due to the limitations regarding simulation times and size of the simulation volumes in AIMD. We note that the Fe-O coordination trend points towards reduction of surface Fe that eventually may lead to accumulation of low amounts of elemental Fe at a later stage.

3. Structural motifs for TiO_2, $TiFeO_3$ and other ternary oxides such as $Ti(FeO_2)_2$ and Ti_2FeO_5 phases appear prominently with increasing O content. The different types of surface oxides may also expand with different thermal expansion coefficients, which can facilitate the H transport through cracks as shown in other work by some of us.[23]

4. H penetration through the sub-surface oxide layers is kinetically hindered under standard conditions and requires either higher thermal energies to overcome multiple activation barriers and/or utilization of catalytically active dopants to reduce the respective barrier heights.

5. Moreover, H trapping in the oxide before reaching the alloy can occur according to the high H migration energy barrier near to the oxide/alloy interface and the surface depth-dependent H binding energies.

6. Adsorbed H_2O can be formed as the H binding is most stable on the topmost surface, where it could then be relatively easily removed via thermal or mechanical methods.

7. Reduction of the top oxide layers under hydrogen atmosphere leads to the formation of structural motifs, such as $FeHO_2$, $Ti_3H_2O_7$, and $Ti(HO)_2$ phases. While the Ti-O coordination notably increases (40.1% in octahedral O6-coordination), Fe is mostly reduced to a 2- or 4-fold coordinated state with O. This implies both, H and Ti-O phases, reduce iron oxides, potentially creating metallic Fe accumulations that can accelerate the initial hydrogenation.

4 Conclusion

We have investigated the early oxidation stages of the TiFe(110) surface with DFT and AIMD methods. After generating and optimizing the lowest energy structures for different oxide coverages on TiFe, we obtained an atomistic level understanding of the likely appearing phases, possible structural motifs and temperature effects.

Adsorbed hydrogen atoms can extract O from the top layers by forming H_2O molecules which could then be removed. The added hydrogen and the Ti-O phases may also reduce the Fe-O phases.

On assessing the energetics of hydrogen dissociation on the oxidized surface, we obtained the minimum energy paths with activation energy barriers of 0.172 eV (dissociation on Fe) to 2.028 eV (dissociation on Ti). Although hydrogen atoms can get adsorbed to the top surface under realistic conditions, the limiting step for hydrogenation is the diffusion through the oxide layer.

In order to reach the bulk interface region, hydrogen hops from one oxygen to another through the sub-surface cavities facing several high energy activation barriers (≥ 1.4 eV). We could find only one path where the migration from the sub-surface O to a metallic site at the bulk interface is exothermic with a reasonable activation barrier of 0.872 eV. The highest energy barrier (1.926 eV) for this diffusion path lies with the penultimate sub-surface H migration. We also followed an alternate path with a lower overall reaction energy which resulted in higher activation barriers for the initial and final H migration steps.

The implication for activation methods therefore is to assist hydrogen to overcome the energy barriers by thermo-chemical approaches and/or mechanical treatment to aid removal of the near-surface oxide layer. Another option is involvment of catalytically active dopants (e.g. transition metals) to lower the activation barriers, which will be explored by us in a future study.

References

[1] M. Hirscher, V. A. Yartys, M. Baricco, J. Bellosta von Colbe, D. Blanchard, R. C. Bowman, D. P. Broom, C. E. Buckley, F. Chang, P. Chen, Y. W. Cho, J. C. Crivello, F. Cuevas, W. I. David, P. E. de Jongh, R. V. Denys, M. Dornheim, M. Felderhoff, Y. Filinchuk, G. E. Froudakis, D. M. Grant, E. M. A. Gray, B. C. Hauback, T. He, T. D. Humphries, T. R. Jensen, S. Kim, Y. Kojima, M. Latroche, H. W. Li, M. V. Lototskyy, J. W. Makepeace, K. T. Møller, L. Naheed, P. Ngene, D. Noréus, M. M. Nygård, S. ichi Orimo, M. Paskevicius, L. Pasquini, D. B. Ravnsbæk, M. Veronica Sofianos, T. J. Udovic, T. Vegge, G. S. Walker, C. J. Webb, C. Weidenthaler, C. Zlotea, *J. Alloys Compd.* **2020**, *827*, 153548.

[2] F. Zhang, P. Zhao, M. Niu, J. Maddy, *Int. J. Hydrogen Energy* **2016**, *41*, 14535–14552.

[3] C. Pistidda, *Hydrogen* **2021**, *2*, 428–443.

[4] E. Commission, D.-G. for Energy, J. Cihlar, A. Villar Lejarreta, A. Wang, F. Melgar, J. Jens, P. Rio, K. Leun, *Hydrogen generation in Europe: overview of costs and key benefits*, Publications Office, **2021**.

[5] W. Cheng, S. Lee, *Sustainability* **2022**, *14*, 1930.

[6] T. Yusaf, M. Laimon, W. Alrefae, K. Kadirgama, H. A. Dhahad, D. Ramasamy, M. K. Kamarulzaman, B. Yousif, *Applied Sciences* **2022**, *12*, 781.

[7] E. H. Jensen, M. Dornheim, S. Sartori, *Inorganics* **2021**, *9*, 37.

[8] N. Bornemann, GKN's Solid-state hydrogen storage system: Enables for a renewable, residential energy supply, tech. rep., GKN Hydrogen, **2018**.

[9] E. M. Dematteis, N. Berti, F. Cuevas, M. Latroche, M. Baricco, *Materials Advances* **2021**, *2*, 2524–2560.

[10] GKN Hydrogen, Hydrogen microgrid project operational utilizing GKN Hydrogen's metal hydride hydrogen storage, **2023**, https://einpresswire.com/article/621914498.

[11] J. J. Reilly, R. H. Wiswall, *Inorg. Chem.* **1974**, *13*, 218–222.

[12] T. Schober, D. G. Westlake, *Scr. Metall.* **1981**, *15*, 913–918.

[13] J. Y. Lee, S. M. Byun, C. N. Park, J. K. Park, *J. Less-Common Met.* **1982**, *87*, 149–164.

[14] S. Morris, S. B. Dodd, P. J. Hall, A. J. MacKinnon, L. E. Berlouis, *J. Alloys Compd.* **1999**, *293*, 458–462.

[15] *Hydrogen as a Future Energy Carrier*, (Eds.: A. Züttel, A. Borgschulte, L. Schlapbach), Wiley, **2008**.

[16] H. Emami, K. Edalati, J. Matsuda, E. Akiba, Z. Horita, *Acta Mater.* **2015**, *88*, 190–195.

[17] A. Izanlou, M. K. Aydinol, *Int. J. Hydrogen Energy* **2010**, *35*, 1681–1692.

[18] C. H. Chiang, Z. H. Chin, T. P. Perng, *J. Alloys Compd.* **2000**, *307*, 259–265.

[19] M. W. Davids, M. Lototskyy, A. Nechaev, Q. Naidoo, M. Williams, Y. Klochko, *Int. J. Hydrogen Energy* **2011**, *36*, 9743–9750.

[20] K. Edalati, J. Matsuda, M. Arita, T. Daio, E. Akiba, Z. Horita, *Appl. Phys. Lett.* **2013**, *103*, 143902.

[21] E. I. L. Gómez, K. Edalati, F. J. Antiqueira, D. D. Coimbrão, G. Zepon, D. R. Leiva, T. T. Ishikawa, J. M. Cubero-Sesin, W. J. Botta, *Adv. Eng. Mater.* **2020**, *22*, 2000011.

[22] A. K. Patel, A. Duguay, B. Tougas, C. Schade, P. Sharma, J. Huot, *Int. J. Hydrogen Energy* **2020**, *45*, 787–797.

[23] D. M. Dreistadt, L. Thi-Thu, G. Capurso, J. M. Bellosta von Colbe, A. Santhosh, C. Pistidda, N. Scharnagl, H. Ovri, C. Milanese, P. Jerabek, T. Klassen, J. Jepsen, *J. Alloys Compd.* **2022**, *919*, 165847.

[24] H. S. Chung, J. Y. Lee, *Int. J. Hydrogen Energy* **1986**, *11*, 335–339.

[25] H. Züchner, G. Kirch, *J. Less-Common Met.* **1984**, *99*, 143–150.

[26] H. C. Kim, J. Y. Lee, *Int. J. Hydrogen Energy* **1985**, *10*, 543–545.

[27] D. Khatamian, G. C. Weatherly, F. D. Manchester, C. B. Alcock, *J. Less-Common Met.* **1983**, *89*, 71–76.

[28] P. Selvam, B. Viswanathan, C. S. Swamy, V. Srinivasan, *Int. J. Hydrogen Energy* **1987**, *12*, 245–250.

[29] R. Hempelmann, E. Wicke, *Ber. Bunsen Ges. Phys. Chem.* **1977**, *81*, 425–429.

[30] T. Matsumoto, M. Amano, *Scr. Metall.* **1981**, *15*, 879–883.

[31] T. Schober, *J. Less-Common Met.* **1983**, *89*, 63–70.

[32] G. Kresse, J. Furthmüller, *Comput. Mater. Sci.* **1996**, *6*, 15–50.

[33] G. Kresse, J. Furthmüller, *Phys. Rev. B* **1996**, *54*, 11169–11186.

[34] J. P. Perdew, A. Ruzsinszky, G. I. Csonka, O. A. Vydrov, G. E. Scuseria, L. A. Constantin, X. Zhou, K. Burke, *Phys. Rev. Lett.* **2008**, *100*, 136406.

[35] J. P. Perdew, K. Burke, M. Ernzerhof, *Phys. Rev. Lett.* **1996**, *77*, 3865.

[36] J. P. Perdew, K. Burke, M. Ernzerhof, *Phys. Rev. Lett.* **1997**, *78*, 1396–1396.

[37] P. E. Blöchl, *Phys. Rev. B* **1994**, *50*, 17953–17979.

[38] S. Grimme, J. Antony, S. Ehrlich, H. Krieg, *J. Chem. Phys.* **2010**, *132*, 154104.

[39] K. Momma, F. Izumi, *J. Appl. Crystallogr.* **2008**, *41*, 653–658.

[40] J. D. Hunter, *IEEE Comput. Sci. Eng.* **2007**, *9*, 90–95.

[41] S. Miracle-Sole in (Eds.: S. Miracle-Sole, J. Ruiz, V. Zagrebnov), World Scientific, Singapore, **1999**, pp. 83–101.

[42] S. P. Ong, W. D. Richards, A. Jain, G. Hautier, M. Kocher, S. Cholia, D. Gunter, V. L. Chevrier, K. A. Persson, G. Ceder, *Comput. Mater. Sci.* **2013**, *68*, 314–319.

[43] D. J. Wales, J. P. Doye, *J. Phys. Chem. A* **1997**, *101*, 5111–5116.

[44] Dong C. Liu, Jorge Nocedal, *Math. Program.* **1989**, *45*, 503–528.

[45] N. Metropolis, A. W. Rosenbluth, M. N. Rosenbluth, A. H. Teller, E. Teller, *J. Chem. Phys.* **1953**, *21*, 1087–1092.

[46] G. Henkelman, H. Jónsson, *J. Chem. Phys.* **2000**, *113*, 9978–9985.

[47] G. Henkelman, B. P. Uberuaga, H. Jónsson, *J. Chem. Phys.* **2000**, *113*, 9901–9904.

[48] J. J. Brown, A. J. Page, *J. Chem. Phys.* **2021**, *154*, 124121.

[49] C. Liu, H. Kubota, T. Toyao, Z. Maeno, K. I. Shimizu, *Catal. Sci. Technol.* **2020**, *10*, 3586–3593.

[50] M. Liu, Z. Rong, R. Malik, P. Canepa, A. Jain, G. Ceder, K. A. Persson, *Energy Environ. Sci.* **2015**, *8*, 964–974.

[51] A. Symington, J. Tse, M. Molinari, A. Marmier, S. Parker, *J. Open Source Softw.* **2019**, *4*, 1210.

[52] K. Reuter, M. Scheffler, *Phys. Rev. B* **2002**, *65*, 035406.

[53] K. Reuter, M. Scheffler, *Phys. Rev. B* **2007**, *75*, 049901.

[54] P. J. Linstrom, W. G. Mallard, *J. Chem. Eng. Data* **2001**, *46*, 1059–1063.

[55] S. Nosé, *J. Chem. Phys.* **1984**, *81*, 511–519.

[56] D. Waroquiers, J. George, M. Horton, S. Schenk, K. A. Persson, G. M. Rignanese, X. Gonze, G. Hautier, *Acta Crystallogr. B* **2020**, *76*, 683–695.

[57] A. P. Bartók, R. Kondor, G. Csányi, *Phys. Rev. B* **2013**, *87*, 184115.

[58] A. P. Bartók, R. Kondor, G. Csányi, *Phys. Rev. B* **2013**, *87*, 219902.

[59] A. P. Bartók, R. Kondor, G. Csányi, *Phys. Rev. B* **2017**, *96*, 019902.

[60] L. Himanen, M. O. Jäger, E. V. Morooka, F. Federici Canova, Y. S. Ranawat, D. Z. Gao, P. Rinke, A. S. Foster, *Comput. Phys. Commun.* **2020**, *247*, 106949.

[61] S. De, A. P. Bartók, G. Csányi, M. Ceriotti, *Phys. Chem. Chem. Phys.* **2016**, *18*, 13754–13769.

[62] Z. Łodziana, *Front. Energy Res.* **2021**, *9*, 719375.

[63] V. B. Oliveira, C. A. G. Beatrice, R. M. L. Neto, W. B. Silva, L. A. Pessan, W. J. Botta, D. R. Leiva, *Mater. Res.* **2021**, *24*, e20210204.

[64] S. Kumar, G. P. Tiwari, S. Sonak, U. Jain, N. Krishnamurthy, *Energy* **2014**, *75*, 520–524.

[65] L. E. Vega, D. R. Leiva, R. M. Leal Neto, W. B. Silva, R. A. Silva, T. T. Ishikawa, C. S. Kiminami, W. J. Botta, *Int. J. Hydrogen Energy* **2018**, *43*, 2913–2918.

[66] L. Schlapbach, T. Riesterer, *10.1007/BF00820257* **1983**, *32*, 169–182.

[67] A. K. Patel, D. Siemiaszko, J. Dworecka-Wójcik, M. Polański, *Int. J. Hydrogen Energy* **2022**, *47*, 5361–5371.

[68] S. De, A. P. Bartók, G. Csányi, M. Ceriotti, *Phys. Chem. Chem. Phys.* **2016**, *18*, 13754–13769.

[69] A. Jain, S. P. Ong, G. Hautier, W. Chen, W. D. Richards, S. Dacek, S. Cholia, D. Gunter, D. Skinner, G. Ceder, K. A. Persson, *APL Mater.* **2013**, *1*, 011002.

[70] H. Zhang, B. Chen, J. F. Banfield, G. A. Waychunas, *Phys. Rev. B* **2008**, *78*, 214106.

[71] M. Nyman, F. Bonhomme, R. S. Maxwell, T. M. Nenoff, *Chem. Mater.* **2001**, *13*, 4603–4611.